Measurement of instantaneous Eulerian acceleration fields by particle-image accelerometry: Method and accuracy

K. T. CHRISTENSEN & R. J. ADRIAN

Laboratory for Turbulence and Complex Flow

Department of Theoretical and Applied Mechanics

University of Illinois, Urbana, IL 61801

Abstract

Acceleration is a fundamental quantity in fluid mechanics because it reflects the sum of all forces (pressure and viscous) present within the flow. However, measurements of acceleration have been difficult to achieve relative to the ease with which fluid velocity can be measured. A particle-image accelerometer (PIA) has been developed to measure Eulerian acceleration fields by time-differencing successive measurements of the Eulerian velocity field as measured by particle-image velocimetry (PIV). The measurements can also be made in uniformly translating frames. With current video camera technology, it is often not possible to measure the two velocity fields with a time separation sufficiently small enough to permit accurate finite difference approximation of the time derivative. A two-CCD-camera system has been developed to alleviate this limitation. Polarization filtering is utilized to separate the particle images viewed by each camera. The polarization filtering is achieved using cross-polarized light-sheets and a polarization filter just upstream of the imaging optics of the cameras. In this manner, PIV measurements can be achieved easily at time delays several orders of magnitude smaller than the shutter-time of the CCD cameras. The accuracy of the acceleration measurements is determined by numerical finite differencing errors and random noise and bias errors associated with the measurement of velocity. These errors, and methods of compensating for them, are studied.

1 Introduction

The incompressible, constant property Navier–Stokes equation,

$$\frac{\partial u_i}{\partial t} = -u_j \frac{\partial u_i}{\partial x_j} - \frac{1}{r}\frac{\partial p}{\partial x_i} + n \frac{\partial^2 u_i}{\partial x_j \partial x_j}, \tag{1}$$

relates the local rate of change of velocity to the advective acceleration and the net pressure and viscous forces in the flow (respective terms on the right-hand side of (1)). While $\partial u_i/\partial t$ represents the local rate of change of the flow in a fixed reference frame, the fluid-particle acceleration is given by the material derivative of velocity:

$$\frac{\mathrm{D}u_i}{\mathrm{D}t} \equiv \frac{\partial u_i}{\partial t} + u_j \frac{\partial u_i}{\partial x_j}. \tag{2}$$

Thus, the material derivative of velocity provides a means of measuring the net pressure and viscous forces within the flow. Although $\partial u_i/\partial t$ is also influenced by the same forces, their contribution is often masked by the typically dominant advective acceleration defined as the rate of change caused by turbulent eddies being swept passed the point of measurement by a mean flow. One can assess the evolution of the flow in a fixed reference frame by replacing u_j in (2) with a constant convection velocity, yielding a bulk or mean convective derivative. The bulk convective derivative represents the evolution of the structures that, on average, advect at this speed. It is an important way of determining the evolution of the dominant vortical structures of turbulence.

The statistical behavior of the temporal and material derivatives of velocity has been studied in the context of scalar transport mostly through numerical and computational approaches and sparingly via experiment (Yueng, 1997; Hill and Thoroddsen, 1997; Pinsky et al., 2000, for example). In this paper, we present a new experimental technique for measuring instantaneous Eulerian acceleration fields using particle-image velocimetry (PIV). The experimental methodology will be discussed in detail and sample acceleration measurements will be presented from studies in turbulent channel flow (Christensen, 2001). The application of this measurement technique to the *direct* documentation of PIV measurement errors is also presented, and a correction methodology is devised to compensate for the propagation of these errors into the acceleration statistics.

2 Experiment

We refer to the experimental methodology of time-differencing two PIV velocity fields presented herein as *particle-image accelerometry* (PIA). At high Reynolds numbers (Re), it is difficult to adequately resolve the temporal evolution of the flow with standard PIV imaging equipment, primarily due to the limited framing rates of current CCD cameras. Standard PIV cross-correlation cameras have a typical frame rate of 30 Hz. At high Re, the flow would advect completely out of the field of view during this time, making time-derivative calculations impossible. Conversely, fast cameras having frame rates of order 10 kHz usually have lower

spatial resolution, making velocity measurement errors large. Therefore, standard PIV imaging technology must be exploited in a novel manner to allow *both* adequate spatial resolution of the small scales of the flow as well as time-resolved measurements at time delays orders of magnitude smaller than camera frame rates.

With the above constraint in mind, a two-CCD-camera particle-image velocimetry (PIV) arrangement is used in this research to measure velocity fields separated by time delays (t) approaching microseconds. Specifically, a separate PIV measurement is made with each CCD camera (1000×1000 pixels, 8-bit, cross-correlation), such that the second measurement occurs t seconds later relative to the first (the cameras are focused upon identical or overlapping flow domains). Since the repetition rate of Nd:YAG lasers is slow compared to the necessary time delays, the field of view is illuminated by two pairs of Nd:YAG lasers which, in concert, produce four distinct laser pulses (two pulses per CCD camera, each pair offset in time).

An added constraint arises because the shutter time of the CCD cameras is an order of magnitude larger than the time delays considered in this research. Therefore, the particle images meant to be viewed by only one CCD camera must not reach the other CCD camera. Since the seed particles used in this experiment are quite small (~ 1 μm in diameter), light scattered from these particles maintains the polarization of the incident light (Adrian and Early, 1976). This property is exploited by *coding* the scattered light imaged by each camera in a predetermined manner by cross-polarizing the two pairs of light sheets. This methodology is explained in greater detail below in the context of the actual measurement system.

2.1 Optics and imaging

Figure 1 illustrates the optical setup used in this experiment. Four Nd:YAG lasers (New Wave Research Gemini series) are used as illumination sources. The lasers emit 120 mJ pulses at a repetition rate of 15 Hz and have a pulse width of 5 ns. The first two pulses provide illumination for the first camera (lasers and camera are shaded white in Figure 1), while the second two laser pulses illuminate the field of view for the second camera (lasers and camera are shaded gray). The second two laser pulses and the second camera are delayed in time by t using a digital-delay generator such that the second camera views the flow at a slightly later time than the first. In order to distinguish between the sets of pulses, the first two pulses (LP 1,2) are rotated to horizontal polarization while the second two pulses (LP 3,4) are rotated to vertical polarization with half wave plates (HWP) just downstream of the laser cavities. All laser pulses are then combined along a common optical path with a polarization beam splitter acting as a beam combiner (BS1). The horizontally polarized light from LP 1,2 passes through the beam splitter, while the vertically polarized light from LP 3,4 is reflected onto the optical path. All pulses then follow the same optical path: through a standard spherical lens (L1) and then through a standard cylindrical lens (L2) yielding light sheets that are 250-μm thick. Since experimental measurements are performed in the streamwise–wall-normal plane (x_1–x_2) of turbulent channel flow, the resulting light sheets are deflected 90° with a right-angle prism (P) from the x_1–x_3 plane into the x_1–x_2 plane along the spanwise centerline of the channel test section. Great care must be taken to assure that all four light sheets are aligned within the exact same plane of the flow.

The scattered light from the seed particles is imaged onto one of the two CCD cameras, depending on the polarization of the scattered light. A polarizing beam splitter (BS2) guides each polarization to the appropriate camera: the horizontally polarized scattered light is transmitted through the beam splitter and imaged by the first CCD camera (C1), while the

vertically polarized light is reflected by the beam splitter and imaged by the second CCD camera (C2). For near-complete separation of the particle images, standard photographic linear polarization filters are mounted just upstream of each imaging lens, ensuring that any cross-polarization leakage (due to the beam splitter's finite transmission/reflection efficiency ($\cong$ 90%)) is properly rejected before imaging.

The PIV images acquired with the particle-image accelerometer are processed using software detailed in Christensen et al. (2000). Standard two-frame cross-correlation analysis is implemented with a discrete window offset. A one-dimensional three-point Gaussian estimator is used to compute the sub-pixel displacements. The particle images are approximately 3 pixels in diameter.

2.2 Camera alignment

It is clear that, in the present experimental arrangement, the two CCD cameras must be accurately aligned such that their fields of view and magnifications are as identical as possible. Each camera is mounted on a two-dimensional translation stage and a laboratory jack such that each has three independent degrees of freedom of motion. A target is placed within the channel cross-section in the same plane as the light sheet and the first camera is focused and aligned with respect to the target. The second camera is then iteratively aligned with respect to the first camera. Images of the target are acquired with each camera and are correlated with one another, yielding a displacement field that represents the relative alignment and magnification differences between the two cameras. This displacement information is then used to refine the relative positions of the cameras such that the misalignment is minimized.

It is impossible, practically, to achieve perfect alignment between the cameras. For example, a slight rotation of the CCD array with respect to the camera body that is not exactly replicated in the other CCD camera would preclude exact alignment between the two cameras. These slight differences cannot be accounted for in the mechanical alignment procedure outlined above; however, the mechanical adjustments do align the two cameras to within 1 pixel across the 1000 pixel image domain, yielding a full-scale difference of less than 0.1%.

2.3 Timing

Accurate timing of the entire PIV arrangement is also crucial. Since TSI's Insight software is used for all acquisition, it is natural to use this system as the "timing master" for the time-derivative measurement system. Therefore, the first camera and laser pulses (C1 and LP 1,2) are controlled directly by the TSI timing synchronizer. In this way, the timing of the first set of images is always aligned with the acquisition timing of the Insight software. The second camera and second set of laser pulses (C2 and LP 3,4) are controlled by a digital-delay generator (Berkeley Nucleonics). This delay generator accepts an external timing trigger and allows for eight independent outputs (either "rise" pulses of a specified amplitude or square trigger pulses of a specified amplitude and duration). Since all pulses originating from the timing master are square pulses with an amplitude of 5 V and a duration of 10 ms, these characteristics are replicated in the pulses created by the delay generator. The delay generator has a minimum delay time of 200 ns, defining the accuracy of the timing equipment.

The timing sequence of the first camera and laser pulses controlled by the synchronizer is replicated by the delay generator for the second camera and second set of laser pulses, with a simple shift of the entire sequence in time by t. In order to synchronize the first camera and

Table 1. Timing summary for time-derivative measurement system.

	Trigger	Identifier	Timing
Camera 1 and Laser Pulses 1 and 2 Controlled by Synchronizer	Camera 1	T_o	T_o
	Flashlamp 1	--	$T_o + T_{PD} - T_{QS}$
	Q-Switch 1	--	$T_o + T_{PD}$
	Flashlamp 2	--	$T_o + T_{PD} - T_{QS} + Dt$
	Q-Switch 2	--	$T_o + T_{PD} + Dt$
Camera 2 and Laser Pulses 3 and 4 Controlled by Delay Generator (triggered from T_o)	Camera 2	T_1	$T_o + t$
	Flashlamp 3	--	$T_1 + T_{PD} - T_{QS}$
	Q-Switch 3	--	$T_1 + T_{PD}$
	Flashlamp 4	--	$T_1 + T_{PD} - T_{QS} + Dt$
	Q-Switch 4	--	$T_1 + T_{PD} + Dt$

laser pulses with the second camera and laser pulses, the trigger pulse sent to the first camera by the synchronizer (T_o) is used as the external timing trigger for the delay generator. The trigger of the second camera is then offset from T_o by t. The triggering of the second set of laser pulses is then simply a replica of the triggering sequence of the first set of laser pulses, except they are now triggered relative to the second camera trigger, and thus are also offset in time by t. This entire timing sequence is summarized in Table 1. The critical parameters involved in the timing of the camera/laser pairs are the pulse delay time and the Q-switch time. The pulse delay time defines the instant at which the first laser pulse is emitted relative to the triggering of the CCD camera (i.e., the moment at which the first Q-switch is triggered). Based upon this setting, the triggering of the laser flashlamp is adjusted to yield the appropriate Q-switch time.

Finally, time delays between the successive velocity measurements are selected to balance the inherent measurement noise with the actual physics being measured. In addition, the numerical error associated with finite-differencing the data is also considered. The time delays used in this work have been selected such that the velocity differences in the finite-differencing of the data are a fraction of the RMS velocity. This criterion satisfies the need for maximizing the measured signal relative to the measurement noise, while maintaining a velocity difference small enough to minimize the numerical error associated with finite-differencing schemes.

A particle-image accelerometry system has also been proposed by Dong et al. (2001) in which a single video camera is used to capture single-frame, double-pulse PIV images separated in time. Autocorrelation analysis of each image yields two velocity fields separated in time, from which the temporal derivative of velocity is evaluated. The advantage of the Dong et al. (2001) arrangement is that it only consists of a single camera, meaning accurate spatial alignment and timing of the system is rather simple to achieve.

The system presented here is different in a few respects. First, it contains the added flexibility of allowing two-frame cross-correlation analysis of the PIV images since it is constructed around two cross-correlation CCD cameras. The use of two-frame cross-correlation analysis with a window offset greatly increases the accuracy of the velocity measurements, especially in the presence of strong mean gradients, and does not suffer from directional ambiguity problems like autocorrelation analysis. Two-frame cross-correlation analysis also effectively increases the spatial resolution of the measurement since only a single image of each particle appears on a given image frame, allowing one to increase the particle-seeding density

accordingly. This is a crucial characteristic of the present system since high spatial resolution is required to resolve the smaller scales of higher-Reynolds-number turbulence. In addition, since the present system is a two-camera arrangement, one can make two independent measurements of velocity for $t = 0$, allowing *direct* documentation of the measurement errors (See Section 4). One can also perform experiments in convective frames by offsetting the second camera in the mean-flow direction relative to the first. However, the system presented here does require careful spatial alignment of the cameras relative to one another, as well as accurate timing of the entire system.

3 Instantaneous temporal and convective derivatives of velocity

The experiments which form the basis of this work are performed in turbulent channel flow. The working fluid is air and the facility is driven by a centrifugal blower. The apparatus has a channel cross-section of $5.08\ \text{cm} \times 51.44\ \text{cm}$ ($2h \times width$, where h is the half-height of the channel) and a development length of $216h$. Details regarding the flow facility can be found in Christensen (2001). The particle-image accelerometer described in Section 2 is used to measure two-dimensional velocity (u,v) fields in the streamwise–wall-normal (x–y) plane along the channel's spanwise centerline separated by a small time delay, from which the temporal and bulk convective derivatives of velocity are calculated. The measurement domain is $h \times h$ ($2.54\ \text{cm} \times 2.54\ \text{cm}$), and 875 statistically independent pairs of velocity realizations are acquired for a each of several different time delays at $\text{Re}_\tau = u_t h/n = 550$ (u_t is the friction velocity and n is the kinematic viscosity of the fluid).

3.1 Temporal derivative

Figure 2(a) represents an instantaneous velocity realization in the streamwise–wall-normal plane of the channel at $\text{Re}_\tau = 550$, while Figure 2(b) represents the velocity field in the identical field-of-view 200 μs later. A constant advection velocity has been removed from each instantaneous velocity field in order to visualize the vortices that are advecting at this speed. Two vortex cores are visible in each velocity field (they are circled for emphasis). The vortices are thought to be the heads of hairpin/hairpin-like vortices propagating as coherent groups in the streamwise direction. The groups, referred to as hairpin vortex packets, can contain many vortices and extend to nearly twice the outer length scale in the streamwise direction (Adrian, Meinhart and Tomkins, 2000).

The field of the local rate of change of velocity ($\partial u_i/\partial t$) computed from Figures 2(a) and 2(b) is presented in Figure 2(c). A first-order, forward-differencing scheme is used to calculate the temporal derivatives of velocity as

$$\frac{\partial u_i}{\partial t}(x,y,t) \approx \frac{{}^{C2}u_i(x,y,t+t) - {}^{C1}u_i(x,y,t)}{t}, \tag{3}$$

where C1 and C2 refer to the velocity fields measured by cameras 1 and 2, respectively. The circles of Figure 2(a,b) are replicated in the $\partial u_i/\partial t$ field in order to aid in associating dominant velocity time-derivative patterns with the vortices themselves. A clear velocity time-derivative "signature" is associated with each vortex and consists of a strong wall-normal acceleration near

the center of each vortex, coupled with a weak streamwise deceleration at the same location. In addition, a rotational pattern exists within the velocity time-derivative field both upstream and downstream of the strong wall-normal acceleration region. Therefore, the complete rate of change "signature" associated with each vortex appears to be a mushroom-like pattern. A qualitatively-similar pattern vortex rate-of-change pattern results if one uses Taylor's hypothesis to evaluate $\partial u_i/\partial t$, implying that these vortices predominantly advect rather than evolve, remaining relatively frozen in time (Christensen, 2001). This behavior is consistent with Taylor's frozen field hypothesis for small scales.

3.2 Bulk convective derivative

The convective derivative of velocity computed in a frame moving at a constant convection velocity, U_c, is

$$\frac{\mathrm{D}_c u_i}{\mathrm{D}t} \equiv \frac{\partial u_i}{\partial t} + U_c \frac{\partial u_i}{\partial x_j} \approx \frac{u_i(\mathbf{x} + U_c t\mathbf{i}, t + t) - u_i(\mathbf{x}, t)}{t}. \tag{4}$$

It represents the time rate of change of u_i seen by an observer moving at the velocity U_c with respect to the laboratory coordinates. The bulk velocity,

$$U_b(y) = \frac{1}{2h}\int_0^{2h} U(y)\mathrm{d}y, \tag{5}$$

is the average streamwise velocity over the height of the channel. It is representative of the average convection velocity of the eddies across the flow. Derivatives in the bulk reference frame, given by (4) with $U_c = U_b$, will be denoted by $\mathrm{D_b}u_i/\mathrm{D}t$. Moving-frame measurements are achieved by shifting the second CCD camera in the streamwise direction by a distance equivalent to $U_b t$ such that the first velocity measurement represents $u_i(x, y, t)$, and the second velocity measurement represents $u_i(x+U_b t, y, t+t)$. Figure 3 illustrates this moving-frame measurement methodology.

An example of an instantaneous measurement of the bulk convective derivative is shown in Figure 4. Figure 4(a,b) illustrates two instantaneous velocity fields separated in time by t = 1 ms and in the streamwise direction by Δx = 6.06 mm ($=U_b t$). Note that the vector fields presented in Figure 4(a,b) have been plotted in the bulk reference frame. (That is, Figure 4(b) has been shifted in the streamwise direction by $U_b t$) The locations of two transverse vortices have been circled in the velocity fields to highlight their respective spatial extents. From visual inspection of these temporally-separated velocity fields, the vortices remain relatively unchanged during the 1 ms interval between the velocity measurements. Any slight changes from Figure 4(a) and Figure 4(b) are attributable to the evolution of the vortices during the time delay t.

Figure 4(c) presents the instantaneous bulk convective derivative computed from the temporally-separated velocity fields shown in Figure 4(a,b). In contrast to the time derivative result shown in Figure 3(c), the mushroom-like pattern present in the $\partial u_i/\partial t$ field that is coincident with the transverse vortex cores is absent in the bulk convective-derivative field, further supporting the notion that the mushroom pattern is predominantly associated with advection of the small-scale, transverse vortices. Additionally, since the time-derivative field

(Figure 3(c)) and the bulk convective-derivative field (Figure 4(c)) are shown with the same vector scaling, it is clear that the bulk convective derivative is nearly an order of magnitude smaller than the temporal derivative. This comparison lends additional support to the contention that the vortices remain relatively frozen in time. In contrast to the well-defined signature in the time-derivative field, the vortices appear to remain relatively unchanged in the bulk convective frame, apart from rising slightly away from the wall.

4 PIV measurement noise

Differentiation of the PIV velocity data is sensitive to noise, so procedures are needed are necessary to correct for noise contamination. Ideally, when $t = 0$ the velocity fields measured by each camera/laser pair should be identical. However, as with any experimental measurement, they are not identical owing to noise within the measurement system. Therefore, the acceleration measurement system detailed in this paper also lends itself to the documentation of PIV measurement noise by comparison of zero-time-delay velocity measurements.

The *measured* velocity of camera # (# represents camera number, either 1 or 2), ${}^{C\#}\breve{u}_i$, can be written as

$$ {}^{C\#}\breve{u}_i(x,y,t) = \bar{u}_i(x,y,t) + {}^{C\#}n_i(x,y,t), \tag{6} $$

where

$$ \bar{u}_i(x,y,t) = \frac{\int_V u_i(\mathbf{x},t) W(\mathbf{x}-\mathbf{x}_I)\mathrm{d}\mathbf{x}}{\int_V W(\mathbf{x})\mathrm{d}\mathbf{x}} \tag{7} $$

is the best estimate of the volume-averaged velocity measured by the PIV technique and n_i is the noise within the PIV measurement. The weighting function, W, depends on the light intensity in the measurement volume and, weakly, on the velocity (Olsen and Adrian, 2001). Note that in the limit of vanishing noise, the PIV still commits an error due to the volume-averaging effect.

Contributions to the noise include:

- n_R : Random error due to electrical noise within the cameras (assumed to be independent between cameras because of adequate shielding), shot noise which is independent from pixel to pixel and in time, and random error associated with properly locating the centroid of the PIV displacement peak (sub-pixel estimation errors). The random noise is independent of both the velocity and the velocity gradient.
- n_B : Bias errors due to pixel-locking, etc. These bias errors are a function of the measured velocity, u_i, the particle-image size, d_t, relative to the pixel size, d_{pix}, (d_t/d_{pix}), the fill ratio of the CCD camera, and the algorithm used to process the images.
- n_G : Gradient noise due to the local random velocity gradients within the flow. Gradient errors can also be introduced by non-uniform mean particle-image distribution within an interrogation spot, which biases the displacement measurement toward lower or higher

displacements depending upon where the particle images are clustered within an interrogation spot.

These errors have been discussed in Keane and Adrian (1990, 1991, 1992), Prasad et al. (1992) and Westerweel (2000). The collective noise in the measurement is then expressed as

$$n_i = n_i^R + n_i^B + n_i^G . \tag{8}$$

The mean and fluctuating measurement error can also be defined. We choose to fix the velocity field, **u**, and compute mean quantities based upon a conditional average given this field, since the velocity fields may also be random. This gives

$$n_i = \left\langle n_i \middle| \mathbf{u} \right\rangle + n_i' . \tag{9}$$

We can also decompose each noise source into a mean and fluctuating portion yielding

$$n_i^G = \left\langle n_i^G \middle| \mathbf{u} \right\rangle + n_i^{G'} , \tag{10}$$

$$n_i^R = \left\langle n_i^R \middle| \mathbf{u} \right\rangle + n_i^{R'} , \tag{11}$$

and

$$n_i^B = \left\langle n_i^B \middle| \mathbf{u} \right\rangle + n_i^{B'} . \tag{12}$$

Since the random noise is independent of the velocity,

$$\left\langle n_i^R \middle| \mathbf{u} \right\rangle = 0 . \tag{13}$$

If the concentration of particles is constant, then on average, the mean gradient error is also negligible:

$$\left\langle n_i^G \middle| \mathbf{u} \right\rangle = 0 . \tag{14}$$

However, since the bias error is a function of the velocity, the conditional average of the bias error given the velocity in (12) is not negligible.

We can also reason that

$$\left\langle n_i^{R'} n_j^{B'} \right\rangle = 0 ; \left\langle n_i^{R'} n_j^{G'} \right\rangle = 0 ; \left\langle n_i^{G'} n_j^{B'} \right\rangle = 0 \ \forall \ i,j . \tag{15}$$

The statistical losses of correlation presented in (15) follow from the statistical independence of the particle positions, electrical noise sources, and the random fluctuations of the gradients in the

flow. Similarly, the same random and bias fluctuating noise components from *different* cameras are also uncorrelated, giving

$$\left\langle {}^{C1}n_i^{R\prime}\,{}^{C2}n_j^{R\prime}\right\rangle = 0\,;\left\langle {}^{C1}n_i^{B\prime}\,{}^{C2}n_j^{B\prime}\right\rangle = 0\ \ \forall\ \ i,j\,. \tag{16}$$

However, if the cameras are perfectly aligned, the cross-correlation of the fluctuating gradient errors of the two measurements cannot be neglected. In fact, the fluctuating gradient errors of the two cameras should be nearly perfectly correlated since they are a function of the same particle images. Therefore,

$$\left\langle {}^{C1}n_i^{G\prime}\,{}^{C2}n_j^{R\prime}\right\rangle \cong \left\langle {}^{C1}n_i^{G\prime}\,{}^{C1}n_j^{G\prime}\right\rangle = \left\langle {}^{C2}n_i^{G\prime}\,{}^{C2}n_j^{G\prime}\right\rangle \ \forall\ \ i,j \tag{17}$$

when the cameras are perfectly aligned. (Condition (17) would become inaccurate with increasing mis-alignment of the cameras since the gradient noise from the two cameras would quickly become decorrelated.) In addition, a set of equations similar to those in (15) exist for cross-correlations between noises from C1 and C2.

Understanding the limiting behavior of these various noise sources is also important, especially when designing an experiment. For example, the bias error, which is strongly dependent upon the ratio of the particle-image size to the physical size of the pixels of the CCD camera, has the limiting behavior

$$\lim_{d_{pix}\to 0} n_B = 0\,. \tag{18}$$

That is, the bias error associated with pixel resolution that is inadequate to fully resolve the character of the particle images decreases as the physical size of the pixels decreases (relative to the particle-image size). The gradient error, which is a function of the velocity gradient, has the limiting behavior

$$\lim_{\nabla u\to 0} n_G = 0\,. \tag{19}$$

In addition, the fluctuating gradient error disappears in the limit of infinite particle-image density (N_I = mean number of particles per interrogation window)

$$\lim_{N_I\to\infty} n_G' = 0\,, \tag{20}$$

since the volume-averaged velocity within an interrogation volume would then be a *true* average representation of the flow within the sub-domain, accounting for all possible gradient fluctuations.

Documenting the character of the individual noise terms outlined above is difficult, but the collective noise present within a PIV measurement can be determined by considering measurements of velocity using the accelerometer described in this paper when $t = 0$. As

alluded to earlier, in the absence of camera noise, the velocity fields measured by the accelerometer should be identical when $t = 0$. Therefore, zero-time-delay measurements of velocity provide a characterization of some of the measurement uncertainty within the system. Figure 5 presents contours of the magnitude of the instantaneous difference between a pair of zero-time-delay measurements (i.e., $\left|{}^{C2}\breve{\mathbf{u}}(x,y,t) - {}^{C1}\breve{\mathbf{u}}(x,y,t)\right|$). Overlaying the associated instantaneous velocity field shows that regions of large error correlate with strong velocity events in the flow. Large errors occur near the wall where the velocity gradients are most intense, as well as around the circumference of the transverse vortex cores, where the velocity gradients are also quite strong. Therefore, instantaneous differences in the zero-time-delay measurements appear to be associated with strong instantaneous velocity gradients present in the flow.

For $t = 0$, the mean-square of the difference in the measured velocities at $t = 0$ is given by (using (6) and the fact that $\bar{u}_i$ is the same for both cameras at $t = 0$)

$$\left\langle \left({}^{C2}\breve{u}_i(x,y,t) - {}^{C1}\breve{u}_i(x,y,t) \right)^2 \right\rangle = \left\langle \left({}^{C2}n_i(x,y,t) - {}^{C1}n_i(x,y,t) \right)^2 \right\rangle . \tag{20}$$

Using (8) and (10)-(15), (20) becomes

$$\begin{aligned} \left\langle \left({}^{C2}n_i(x,y,t) - {}^{C1}n_i(x,y,t) \right)^2 \right\rangle = & \left\langle \left(\left\langle {}^{C2}n_i^B \middle| \mathbf{u} \right\rangle + {}^{C2}n_i^{B'} \right)^2 + \left({}^{C2}n_i^{R'} \right)^2 + \left({}^{C2}n_i^{G'} \right)^2 \right\rangle \\ & - 2\left\langle \left(\left\langle {}^{C2}n_i^B \middle| \mathbf{u} \right\rangle + {}^{C2}n_i^{B'} + {}^{C2}n_i^{R'} + {}^{C2}n_i^{G'} \right) \left(\left\langle {}^{C1}n_i^B \middle| \mathbf{u} \right\rangle + {}^{C1}n_i^{B'} + {}^{C1}n_i^{R'} + {}^{C1}n_i^{G'} \right) \right\rangle \\ & + \left\langle \left(\left\langle {}^{C1}n_i^B \middle| \mathbf{u} \right\rangle + {}^{C1}n_i^{B'} \right)^2 + \left({}^{C1}n_i^{R'} \right)^2 + \left({}^{C1}n_i^{G'} \right)^2 \right\rangle \end{aligned} \tag{21}$$

The contribution of the mean bias errors to (21),

$$\left\langle \left(\left\langle {}^{C1}n_i^B \middle| \mathbf{u} \right\rangle \right)^2 \right\rangle + \left\langle \left(\left\langle {}^{C2}n_i^B \middle| \mathbf{u} \right\rangle \right)^2 \right\rangle - 2\left\langle \left\langle {}^{C1}n_i^B \middle| \mathbf{u} \right\rangle \left\langle {}^{C2}n_i^B \middle| \mathbf{u} \right\rangle \right\rangle , \tag{22}$$

is negligible because the bias errors associated with the C1 and C2 measurements are nearly equal at $t = 0$. The contribution of the fluctuating gradient errors to (21)

$$\left({}^{C1}n_i^{G'} \right)^2 + \left({}^{C2}n_i^{G'} \right)^2 - 2\left\langle {}^{C1}n_i^{G'}\, {}^{C2}n_i^{G'} \right\rangle , \tag{23}$$

is also negligible based upon (17), since the fluctuating gradient error of each measurement is nearly perfectly correlated (the third term of (23)) assuming negligible mis-alignment of the cameras. In addition, the cross-correlations between fluctuating random and bias noises of the two separate measurements in the second term of (21) are negligible based upon (16). Therefore, (21) becomes

$$\left\langle \left({}^{C2}n_i(\mathbf{x},t) - {}^{C1}n_i(\mathbf{x},t) \right)^2 \right\rangle = \left\langle \left({}^{C1}n_i^{R\prime} \right)^2 \right\rangle + \left\langle \left({}^{C2}n_i^{R\prime} \right)^2 \right\rangle + \left\langle \left({}^{C1}n_i^{B\prime} \right)^2 \right\rangle + \left\langle \left({}^{C2}n_i^{B\prime} \right)^2 \right\rangle. \quad (24)$$

Equation (24) provides a measure of the mean-square *fluctuating* random and bias errors associated with the PIV measurement technique. One can define the mean-square fluctuating measurement error embodying the fluctuating bias and random noises as

$$\left\langle \left(n_i^{RB\prime} \right)^2 \right\rangle \equiv \left\langle \left(n_i^{R\prime} \right)^2 \right\rangle + \left\langle \left(n_i^{B\prime} \right)^2 \right\rangle, \quad (25)$$

and since it is reasonable to assume that the fluctuating errors present within the two separate PIV measurements are, on average, the same, (24) reduces to

$$\left\langle \left({}^{C2}n_i(x,y,t) - {}^{C1}n_i(x,y,t) \right)^2 \right\rangle \cong 2\left\langle \left(n_i^{R\prime} \right)^2 \right\rangle + 2\left\langle \left(n_i^{B\prime} \right)^2 \right\rangle = 2\left\langle \left(n_i^{RB\prime} \right)^2 \right\rangle. \quad (26)$$

Therefore, the root-mean-square of the fluctuating random and bias PIV noise measured using zero-time-delay measurements is given by

$$s_{ni} \equiv \left\langle \left(n_i^{RB\prime} \right)^2 \right\rangle^{1/2} \cong \frac{1}{\sqrt{2}} \left\langle \left({}^{C2}\breve{u}_i(x,y,t) - {}^{C1}\breve{u}_i(x,y,t) \right)^2 \right\rangle^{1/2}. \quad (27)$$

In turbulent channel flow, where the streamwise direction (x) is statistically homogeneous, one can use (27) to compute the root-mean-square (RMS) profiles of the fluctuating measurement noises as a function of wall-normal position (y). Figure 6 illustrates the RMS profiles of n_1' (fluctuating noise associated with the measurement of u_1) and n_2' (fluctuating noise associated with the measurement of u_2) as a function of y. The RMS values in Figure 6 have been rescaled by $M\Delta t$ (where M is the magnification of the measurement and Δt is the PIV time delay). Therefore, the profiles in Figure 6 represent the RMS noise of the particle-displacement measurement in terms of pixels rather than the noise associated with the velocity itself, as defined by the decomposition in (6) (This conversion is done as a convenience for comparing to previous results in the literature). Near the wall, the RMS noise is quite large, while farther away from the wall the RMS values of s_{n1} and s_{n2} quickly asymptote toward a constant value. The outer-layer behavior of both noise profiles is expected since one would anticipate minimal dependence of the noise upon wall normal position, since the RMS noise presented in Figure 6 represents the contributions of the fluctuating random and bias errors (eqn. (26)).

The near-wall behavior of the streamwise noise, however, is a bit suprising because of its strong dependence upon wall-normal position. According to the arguments presented above, the zero-time-delay measurements should only represent the fluctuating random and bias errors. However, neither of these errors is a direct function of the mean velocity gradient which renders the wall-normal direction inhomogeneous. Scaling the streamwise RMS noise profile with the

mean velocity, RMS velocity, and the mean velocity gradient does not remove the wall-normal dependence seen in Figure 6. Therefore, the wall-normal dependence of the streamwise RMS profile cannot be directly attributed to one of these effects. In addition, estimates of the gradient error presented in Keane and Adrian (1992) show that any error associated with the mean velocity gradient should be an order of magnitude smaller than what is observed in Figure 6. The effect of gradient error introduced by relative mis-alignment of the cameras was also considered. However, any error introduced by mis-alignment was found to be an order of magnitude smaller than the behavior noted near the wall in Figure 6. It is possible that close to the wall, an increased number of invalid vectors is skewing the RMS profile toward higher values. It is also possible, though not expected, that one or more of the cross-correlations of fluctuating noise neglected in the analysis is, for some reason, larger than believed. At this time, we cannot offer a clear explanation of the near-wall behavior of the streamwise RMS noise.

Prasad et al. (1992) showed that the random error associated with PIV measurements in zero gradient fields is proportional to the particle-image size (d_t):

$$\text{Random Error} \propto c d_t \,, \tag{28}$$

where c is a proportionality constant between 0.05 and 0.07. In addition, Westerweel (2000) theoretically studied the measurement precision and also found that, for constant image density, the random error is proportional to the particle-image diameter, d_t. For the PIV experiments considered herein, where the particle-image diameter is 2.5-3 pixels, the random error as defined in (28) would be approximately 0.125-0.15 pixels. If the *global* RMS noise is computed from the zero-time-delay measurements (that is, averaged in y in addition to x), then the baseline level of noise within the measurement system in this particular turbulent environment is 0.16 and 0.13 pixels in u_1 and u_2, respectively. These values of the random error are dominated by the low gradient, core region of the channel ($y/h > 0.1$). They are consistent with the RMS values of the noise estimated from (28). Note that this error exists even if the bias error is reduced to zero.

5 Correcting time-derivative statistics for noise

Now let us consider the propagation of measurement noise into the statistics of the acceleration. Using (3), the mean-square of the measured temporal derivative of velocity is

$$\left\langle \left(\frac{\partial \breve{u}_i}{\partial t}(x,y,t) \right)^2 \right\rangle = \left\langle \breve{a}_i^{\,2} \right\rangle \approx \left\langle \frac{\left({}^{C2}\breve{u}_i(x,y,t+t) - {}^{C1}\breve{u}_i(x,y,t) \right)^2}{t^{\,2}} \right\rangle, \tag{29}$$

where, from (6),

$${}^{C1}\breve{u}_i(x,y,t) = \bar{u}_i(x,y,t) + {}^{C1}n_i(x,y,t) \tag{30}$$

and

$${}^{C2}\breve{u}_i(x,y,t+t) = \bar{u}_i(x,y,t+t) + {}^{C2}n_i(x,y,t+t). \tag{31}$$

(Note that the camera designation is absent from the volume-averaged velocity on the right-hand side of (30) and (31) since all of the camera dependence is embedded within the noise) Substituting (30) and (31) into (29) and expanding gives

$$\left\langle \breve{a}_i^2 \right\rangle = \frac{1}{t^2}\left\langle \begin{array}{l} \left(\bar{u}_i(x,y,t+t)-\bar{u}_i(x,y,t)\right)^2 \\ +2\left(\bar{u}_i(x,y,t+t)-\bar{u}_i(x,y,t)\right)\left({}^{C2}n_i(x,y,t+t)-{}^{C1}n_i(x,y,t)\right) \\ +\left({}^{C2}n_i(x,y,t+t)-{}^{C1}n_i(x,y,t)\right)^2 \end{array} \right\rangle . \tag{32}$$

The first term of (32) represents the best estimate of the mean-square velocity time-derivative,

$$\left\langle a_i^2 \right\rangle = \left\langle \frac{\left(\bar{u}_i(x,y,t+t)-\bar{u}_i(x,y,t)\right)^2}{t^2} \right\rangle , \tag{33}$$

while the remaining terms of (32) represent noise that has propagated into the mean-square estimate. The second term of (32), the cross-correlation between the velocity difference and the difference of the measurement noise, can be expanded as

$$\begin{aligned} \left\langle \left(\bar{u}_i(x,y,t+t)-\bar{u}_i(x,y,t)\right)\left(n_i^{C2}(x,y,t+t)-n_i^{C1}(x,y,t)\right) \right\rangle &= \left\langle \left(\bar{u}_i(x,y,t+t)-\bar{u}_i(x,y,t)\right)\left({}^{C2}n_i^B+{}^{C2}n_i^R+{}^{C2}n_i^G\right) \right\rangle \\ &\quad -\left\langle \left(\bar{u}_i(x,y,t+t)-\bar{u}_i(x,y,t)\right)\left({}^{C1}n_i^B+{}^{C1}n_i^R+{}^{C1}n_i^G\right) \right\rangle \end{aligned} , \tag{34}$$

where the C1 superscript on n_i implies evaluation at (x, y) and t and C2 implies evaluation at (x, y) and $(t+t)$. The only noise component that is correlated with the fluid velocity is the bias error. Therefore, (34) reduces to

$$\begin{aligned} \left\langle \left(\bar{u}_i(x,y,t+t)-\bar{u}_i(x,y,t)\right)\left({}^{C2}n_i(x,y,t+t)-{}^{C1}n_i(x,y,t)\right) \right\rangle &= \left\langle \left(\bar{u}_i(x,y,t+t)-\bar{u}_i(x,y,t)\right){}^{C2}n_i^B \right\rangle \\ &\quad -\left\langle \left(\bar{u}_i(x,y,t+t)-\bar{u}_i(x,y,t)\right){}^{C1}n_i^B \right\rangle \end{aligned} . \tag{35}$$

Further, since t is relatively small, the bias error is nearly identical between C1 and C2, implying that the cross-correlation between the velocity difference and the noise in (32) is negligible.

On the other hand, the third term of (32) is not negligible. This term is quite similar to the noise difference considered in Section 4; however, we now must consider small, but non-zero t. Expanding the third term of (32) and again assuming that the different fluctuating noises for a *given* camera are uncorrelated (equation (15) of Section 4) yields

$$\begin{aligned} \left\langle \left({}^{C2}n_i(x,y,t+t)-{}^{C1}n_i(x,y,t)\right)^2 \right\rangle &= \left\langle \left(\left\langle {}^{C2}n_i^B \middle| \mathbf{u} \right\rangle + {}^{C2}n_i^{B'}\right)^2 + \left({}^{C2}n_i^{R'}\right)^2 + \left({}^{C2}n_i^{G'}\right)^2 \right\rangle \\ &\quad -2\left\langle \left(\left\langle {}^{C2}n_i^B \middle| \mathbf{u} \right\rangle + {}^{C2}n_i^{B'} + {}^{C2}n_i^{R'} + {}^{C2}n_i^{G'}\right)\left(\left\langle {}^{C1}n_i^B \middle| \mathbf{u} \right\rangle + {}^{C1}n_i^{B'} + {}^{C1}n_i^{R'} + {}^{C1}n_i^{G'}\right) \right\rangle \\ &\quad +\left\langle \left(\left\langle {}^{C1}n_i^B \middle| \mathbf{u} \right\rangle + {}^{C1}n_i^{B'}\right)^2 + \left({}^{C1}n_i^{R'}\right)^2 + \left({}^{C1}n_i^{G'}\right)^2 \right\rangle \end{aligned} . \tag{36}$$

The first and third terms of (36) embody the autocorrelations of the measurement noise within a given velocity measurement, while the second term of (36) represents the cross-correlations of the noise within the two separate velocity measurements. This expression can be further simplified using the assumption that the fluctuating random and bias noises from different cameras are also uncorrelated (equation (16) in Section 4). In addition, since the time delay is small compared to the mean advection time-scale of the flow, the *mean* bias errors of the different cameras are still nearly identical, implying that the condition noted in equation (22) in Section 4 is still valid (That is, the mean bias errors negate one-another in (36)). However, unlike the zero-time-delay case (eqn. (23)), the contribution of the fluctuating gradient errors (GC)

$$\mathrm{GC} = \left({}^{C1}n_i^{G\prime} \right)^2 + \left({}^{C2}n_i^{G\prime} \right)^2 - 2\left\langle {}^{C1}n_i^{G\prime}\, {}^{C2}n_i^{G\prime} \right\rangle, \tag{37}$$

cannot be neglected in the case of non-zero t. The third term of (37), which was assumed to be nearly perfectly correlated in the zero-time-delay case, is appreciably smaller for non-zero t and therefore cannot negate the effect of the first two terms of (37). This decorrelation is attributable to the fact that, since the time-delay, t, is much larger than the PIV time-delay, Δt, the particles present in a given interrogation window during the first velocity measurement will have advected out of that same interrogation window once the second velocity measurement is made t seconds later. Therefore, gradient errors associated with the particle-image distribution in spatially coincident interrogation windows of the two velocity measurements will be minimally correlated. Applying the above conditions to (36) gives

$$\left\langle \frac{\left({}^{C2}\breve{u}_i(x,y,t+t) - {}^{C1}\breve{u}_i(x,y,t) \right)^2}{t^2} \right\rangle = \frac{1}{t^2} \left\langle \begin{array}{l} \left(\bar{u}_i(x,y,t+t) - \bar{u}_i(x,y,t) \right)^2 \\ + \left({}^{C1}n_i^{R\prime} \right)^2 + \left({}^{C2}n_i^{R\prime} \right)^2 \\ + \left({}^{C1}n_i^{B\prime} \right)^2 + \left({}^{C2}n_i^{B\prime} \right)^2 \\ + \mathrm{GC} \end{array} \right\rangle. \tag{38}$$

Therefore, the measured mean-square time-derivative embodies noise contributions due to the fluctuating random and bias errors along with a fluctuating gradient error contribution. The random and bias errors can be accounted for using zero-time-delay measurements as discussed in Section 4. Combining (32) and (38), the best estimate of the *true* mean-square acceleration is given by

$$\left\langle a_i^2 \right\rangle \cong \frac{1}{t^2} \left\langle \left({}^{C2}\breve{u}_i(\mathbf{x},t+t) - {}^{C1}\breve{u}_i(\mathbf{x},t) \right)^2 \right\rangle - \frac{2}{t^2} \left\langle \left(n_i^{RB\prime} \right)^2 \right\rangle. \tag{39}$$

The approximate sign in (39) reflects the fact that the contribution of the fluctuating gradient error is still present in the mean-square result since it cannot be accounted for using the zero-time-delay results. However, estimates of the gradient noise presented in Keane and Adrian

(1992) indicate this it is appreciably smaller than the errors associated with the random and bias noise accounted for in the second term of the right-hand side of (39).

Equation (39) can now be used to compensate the estimate of the mean-square temporal derivative for the fluctuating measurement noise embedded within the velocity measurements. For example, Figure 7(a) presents the RMS profiles of $\partial u_i/\partial t$ as defined in (29) at $Re_\tau = 550$. They are computed from 875 independent realizations of $\partial u_i/\partial t$. This "raw" data is then corrected for the presence of random noise in the measurement using (38) and is shown in Figure 7(b). Near the wall, where the measurement noise is particularly strong (see Figure 6), the character of the streamwise temporal derivative changes markedly. In the outer region ($y/h > 0.3$), the influence of the measurement noise is not as noticeable. Note that the corrected result still represents the acceleration associated with the filtered (volume-averaged) velocity, $\overline{u}_i$, not the true velocity. Hence, the filtered acceleration converges to the true acceleration only in the limit of sufficiently small measurement volumes. Fortunately, the filtered acceleration fields are of direct interest in large-eddy simulation research.

6 Summary

A new experimental methodology, particle-image accelerometry, has been introduced for the measurement of time-derivative fields in fluid mechanics. A two-CCD-camera PIV arrangement allows one to acquire time-resolved velocity fields in high-Reynolds-number turbulence where time delays on the order of microseconds are required for accurate characterization of small-scale flow dynamics. Sample acceleration measurements in turbulent channel flow indicate that the dominant vortical structures remain relatively frozen in time (i.e., evolve on a very long time scale). This contention is supported by the fact that the magnitude of the bulk convective derivative is nearly an order of magnitude smaller than the temporal derivative of velocity, implying that advective effects dominate $\partial u_i/\partial t$.

This new experimental tool also provides a direct measure of the random errors associated with the PIV measurement technique. It is found that the fluctuating error in the PIV measurement is of the order 0.15 pixels in both the streamwise and wall-normal velocity estimates. This direct measure of the experimental error is similar to the well-established random error estimates of Prasad et al. (1992) and Westerweel (2000) where the random error was shown to be proportional to the particle-image diameter for constant image density. It must be emphasized that the random error is a function of the noise level of the video camera and is non-zero even in the limit of vanishing mean bias error.

Finally, a methodology is presented that allows one to remove these errors from the acceleration statistics based upon the zero-time-delay velocity measurements. Although the influence of the mean bias error is a direct function of the time delay used, for small time delays the fluctuating errors dominate the noise that propagates into the acceleration statistics.

Acknowledgements

The financial support of the National Science Foundation and the Air Force Office of Scientific Research is gratefully acknowledged. The first author was partially supported by a Graduate Fellowship from the National Science Foundation.

References

Adrian R J; Meinhart C D; Tomkins C D (2000) Vortex Organization in the Outer Region of the Turbulent Boundary Layer. *J. Fluid Mech.* **422**, 1-54.

Adrian R J; Earley W L (1976) Evaluation of Laser-Doppler Velocimeter Performance using Mie Scattering Theory. *Technical Report 479*, Department of Theoretical and Applied Mechanics, University of Illinois at Urbana-Champaign.

Christensen K T; Soloff S M; Adrian R J (2000) PIV Sleuth–Integrated Particle-Image Velocimetry Interrogation/Validation Software. *Technical Report 943*, Department of Theoretical and Applied Mechanics, University of Illinois at Urbana-Champaign.

Christensen K T (2001) Experimental Investigation of Acceleration and Velocity Fields in Turbulent Channel Flow. PhD Thesis, Department of Theoretical and Applied Mechanics, University of Illinois, Urbana, Ill. USA.

Dong P; Hsu T-Y; Atsavapranee P; Wei T (2001) Digital Particle Image Accelerometry. *Exp. Fluids*, **30**, 626-632.

Hill R J; Thoroddsen S T (1997) Experimental Evaluation of Acceleration Correlations for Locally Isotropic Turbulence. *Phys. Rev. E*, **55** (2), 1600-1606.

Keane R D; Adrian R J (1990) Optimization of Particle Image Velocimeters: I. Double Pulsed Systems. *Meas. Sci. Technol.* **1**, 1202-1215.

Keane R D; Adrian R J (1991) Optimization of Particle Image Velocimeters: II. Multiple Pulsed Systems. *Meas. Sci. Technol.* **2**, 963-974.

Olsen M G; Adrian R J (2001) Measurement Volume Defined by Peak-Finding Algorithms in Particle-Image Velocimetry. *Meas. Sci. Technol.* **12**, N14-N16.

Pinsky M; Khain A; Tsinober A (2000) Accelerations in Isotropic and Homogeneous Turbulence and Taylor's Hypothesis. *Phys. Fluids*, **12** (12), 3195-3204.

Prasad A K; Adrian R J; Landreth C C; Offutt P W (1992) Effect of Resolution on the Speed and Accuracy of Particle-Image Velocimetry Interrogation. *Exp. Fluids*, **13**, 105-116.

Westerweel J (2000) Theoretical Analysis of the Measurement Precision in Particle Image Velocimetry. *Exp. Fluids*, **29**, S3-S12.

Yueng P K (1997) One- and Two-Dimensional Lagrangian Acceleration Correlations in Numerically Simulated Homogeneous Turbulence. *Phys. Fluids*, **9** (10), 2981-2990.

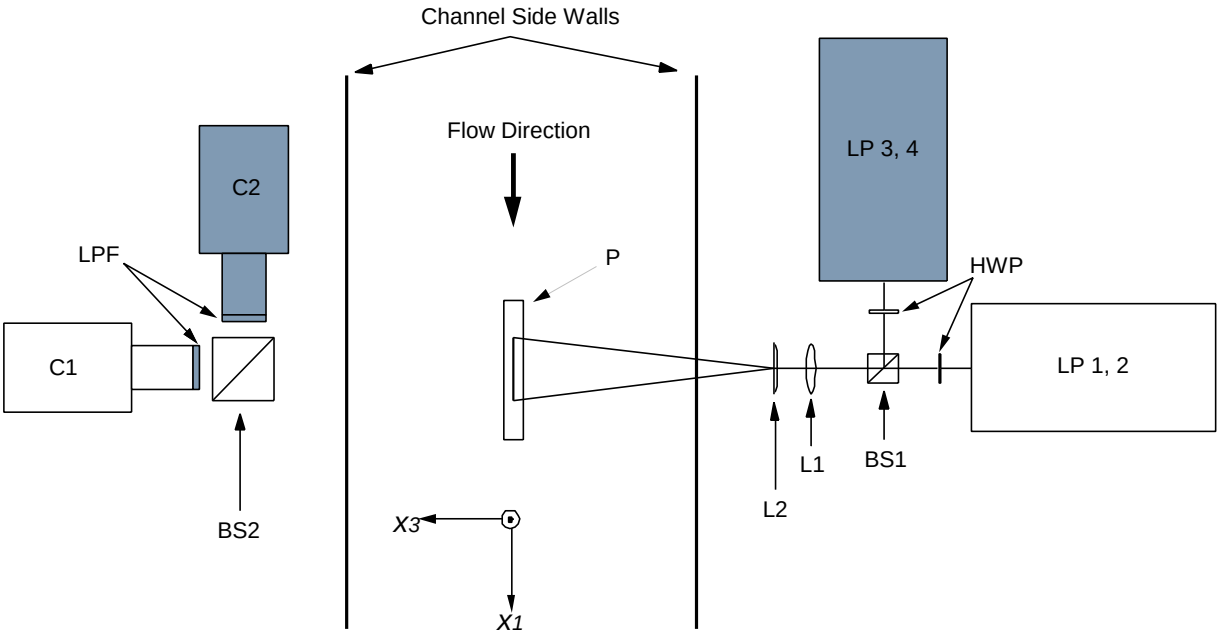

BS1 : High-Energy Polarizing Beam Combiner
BS2 : Polarizing Beam Splitter
C1 : CCD Camera #1 (synchronized with LP 1, 2)
C2 : CCD Camera #2 (synchronized with LP 3, 4)
HWP : Half Wave Plate
L1 : Spherical Lens (1 diopter)
L2 : Cylindrical Lens (30 mm focal length)
LPF : Linear Polarization Filter
LP 1, 2 : Laser pulses 1 and 2 (horizontally polarized)
LP 3, 4 : Laser pulses 3 and 4 (vertically polarized)
P : Prism

Figure 1. Experimental setup, viewed from above. Shading of lasers and cameras indicates which laser pulses are synchronized with which camera.

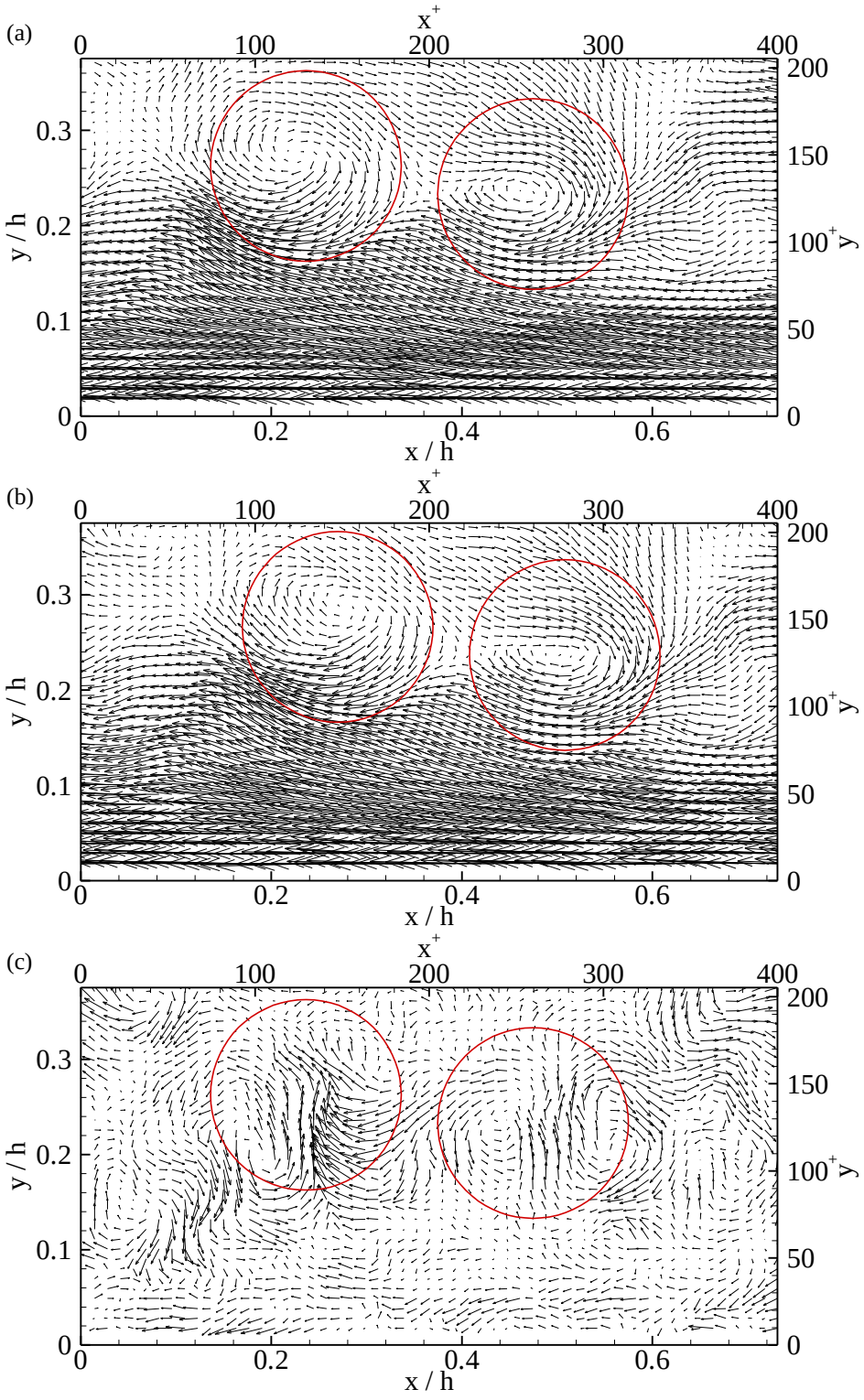

Figure 2. Example of instantaneous velocity and velocity time-derivative fields in the streamwise–wall-normal plane of turbulent channel flow at $Re_\tau = 550$. (a) Instantaneous velocity; (b) instantaneous velocity temporally separated from (a) by $t = 200$ μs; (c) $\partial u_i/\partial t$.

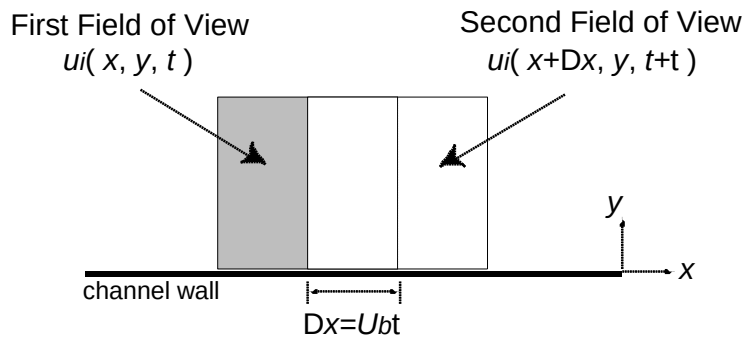

Figure 3. Schematic of bulk convective derivative measurements made in a moving reference frame. The second field of view is $U_b t$ further downstream from the first field of view, where t is the time delay between the measurements made at the first and second fields of view.

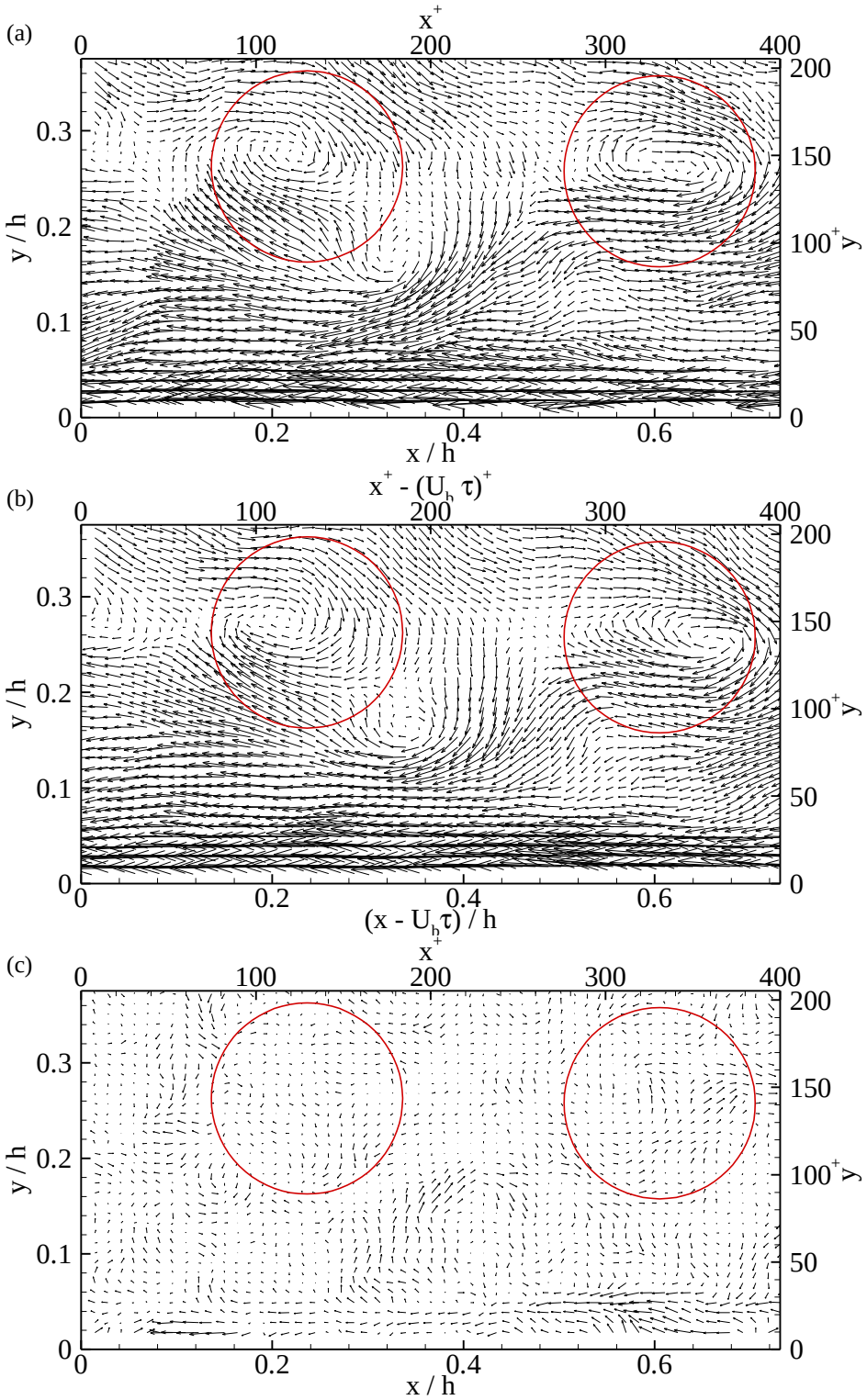

Figure 4. Example of instantaneous velocity and velocity bulk-convective-derivative fields in the streamwise–wall-normal plane of turbulent channel flow at $Re_\tau = 550$. (a) Instantaneous velocity; (b) instantaneous velocity temporally separated from (a) by $t = 1$ ms (streamwise coordinate has been shifted upstream by $U_b t$ in order to center the flow in the bulk reference frame); (c) $D_b u_i / Dt$.

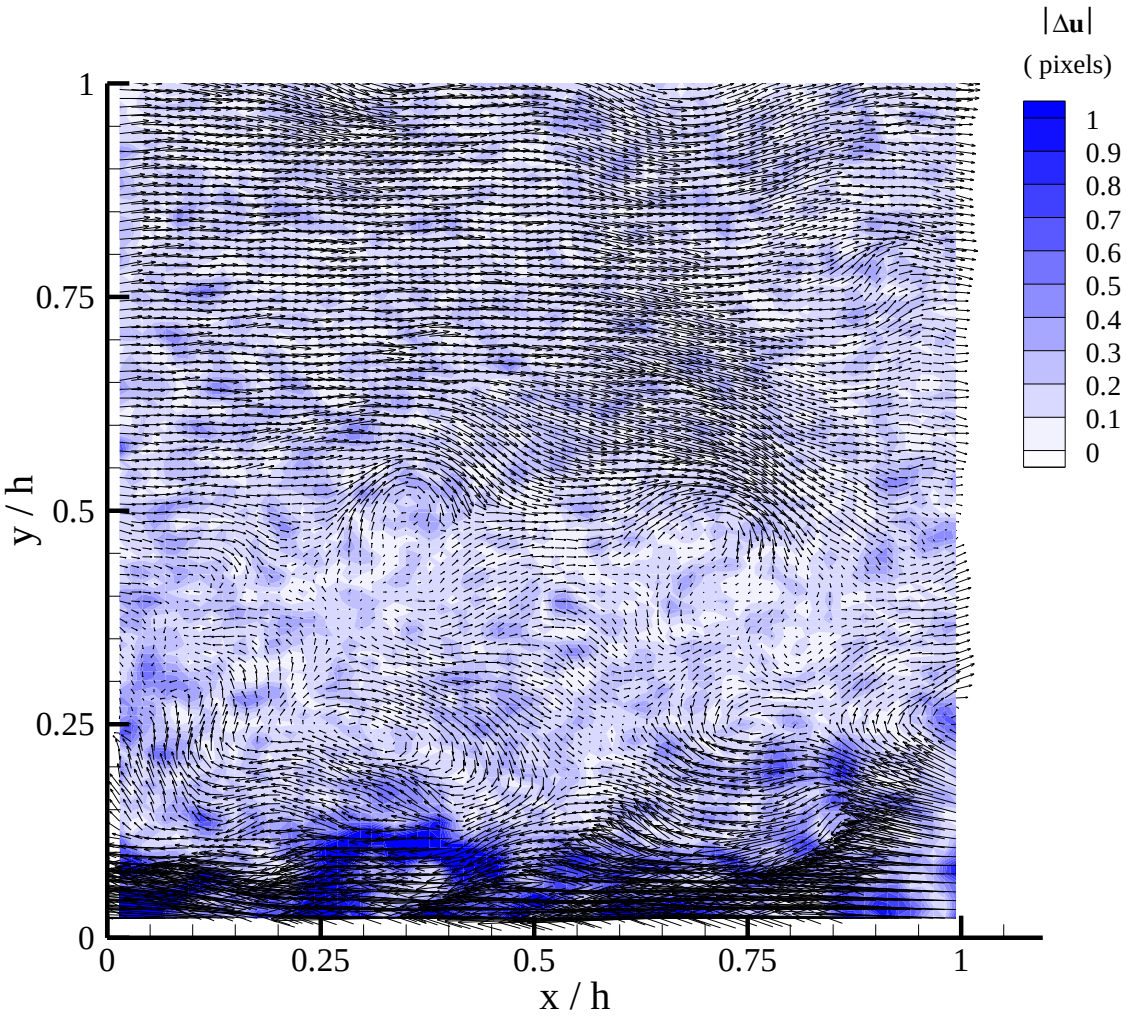

Figure 5. Instantaneous velocity field with contours of $|\Delta\mathbf{u}| = \left|\left({}^{C2}\breve{\mathbf{u}}(x,y,t) - {}^{C1}\breve{\mathbf{u}}(x,y,t)\right)\right|_{t=0}$ plotted in the background. There is strong spatial coincidence between strong velocity gradients and large measurement errors.

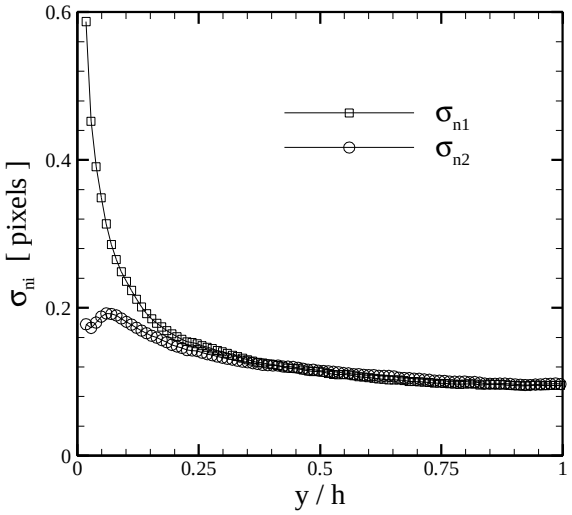

Figure 6. RMS profiles of the fluctuating noise, s_{n1} and s_{n2}, as a function of wall-normal position (y).

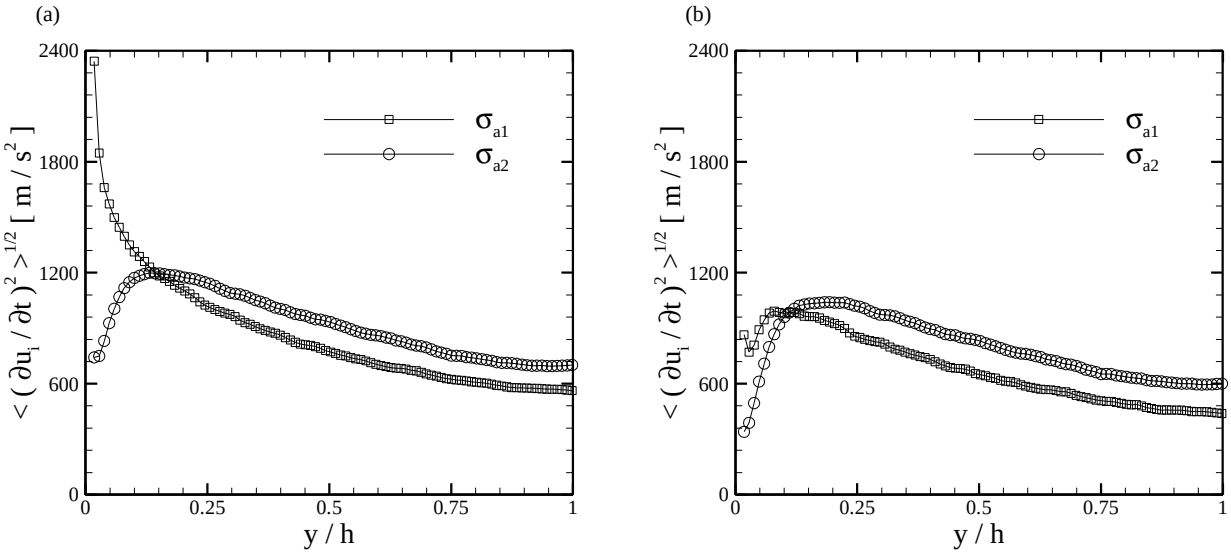

Figure 7. RMS profiles of $\partial u_i/\partial t$ as a function of wall-normal position (y). (a) RMS profiles of $\partial u_i/\partial t$ with no noise correction; (b) RMS profiles of $\partial u_i/\partial t$ with fluctuating noise compensation defined by equation (39).